The Astrophysical Journal, 849:154 (13pp), 2017 November 10 https://doi.org/10.3847/1538-4357/aa93f6

ALMA Pinpoints a Strong Overdensity of U/LIRGs in the Massive Cluster XCS J2215 at $z = 1.46$

Stuart M. Stach[1], A. M. Swinbank[1], Ian Smail[1], Matt Hilton[2], J. M. Simpson[3], and E. A. Cooke[1]
[1] Centre for Extragalactic Astronomy, Department of Physics, Durham University, South Road, Durham, DH1 3LE, UK; stuart.m.stach@durham.ac.uk
[2] Astrophysics and Cosmology Research Unit, School of Mathematics, Statistics and Computer Science, University of KwaZulu-Natal, Durban 4041, South Africa
[3] Academia Sinica Institute of Astronomy and Astrophysics, No. 1, Section 4, Roosevelt Road, Taipei 10617, Taiwan
Received 2017 May 2; revised 2017 October 9; accepted 2017 October 12; published 2017 November 10

Abstract

We surveyed the core regions of the $z = 1.46$ cluster XCS J2215.9−1738 with the Atacama Large Millimeter Array (ALMA) and the MUSE-GALACSI spectrograph on the Very Large Telescope (VLT). We obtained high spatial resolution observations with ALMA of the 1.2 mm dust continuum and molecular gas emission in the central regions of the cluster. These observations detect 14 significant millimeter sources in a region with a projected diameter of just ∼500 kpc (∼1′). For six of these galaxies, we also obtain ^{12}CO(2–1) and ^{12}CO(5–4) line detections, confirming them as cluster members, and a further five of our millimeter galaxies have archival ^{12}CO(2–1) detections, which also place them in the cluster. An additional two millimeter galaxies have photometric redshifts consistent with cluster membership, although neither show strong line emission in the MUSE spectra. This suggests that the bulk ($\geqslant 11/14$, ∼80%) of the submillimeter sources in the field are in fact luminous infrared galaxies lying within this young cluster. We then use our sensitive new observations to constrain the dust-obscured star formation activity and cold molecular gas within this cluster. We find hints that the cooler dust and gas components within these galaxies may have been influenced by their environment, reducing the gas reservoir available for their subsequent star formation. We also find that these actively star-forming galaxies have dynamical masses and stellar population ages expected for the progenitors of massive, early-type galaxies in local clusters, potentially linking these populations.

Key words: galaxies: clusters: individual (XMMXCS J2215.9–1738) – galaxies: evolution – galaxies: formation

1. Introduction

Galaxy clusters present a convenient laboratory for the study of environmental influences on galaxy formation and evolution due to the large variety in environments within a relatively small observable area, from the high-density cores to the low-density outskirts. Observational studies of clusters in the local universe show that their cores are dominated by metal-rich, gas-poor early-type (lenticulars, or S0s, and ellipticals) galaxies with little or no current star formation activity. In contrast, late-type, actively star-forming disk galaxies are found preferentially in the outskirts of clusters and in the surrounding lower-density field, yielding a so-called "morphology–density" relation (Dressler 1980; Bower et al. 1992; Whitmore et al. 1993; Bamford et al. 2009).

This correlation of galaxy star formation activity and morphology with environment in the local universe (e.g., Lewis et al. 2002; Gomez et al. 2003; Balogh et al. 2004; Kodama et al. 2004) is suggestive of environmental processes being at least partly responsible for the quenching of star formation in the early-type galaxies in high-density regions. Potential environmental processes that could drive this include galaxies interacting with the intracluster medium (ICM), causing ram pressure stripping of their interstellar gas (Gunn & Gott III 1972) or "strangulation," where the continued accretion of gas from their surroundings is cut off (Larson et al. 1980); galaxy mergers leading to dramatic changes in the galaxy's structure and the triggering of a starburst which rapidly consumes their gas (Merritt 1983); and tidal interactions, which can enhance star formation (Aguilar & White 1985). Ultimately, each of these processes acts to reduce the gas supply and eventually shut off star formation, and all act preferentially on galaxies in higher density regions.

At higher redshift, it has been shown that the fraction of blue star-forming disk galaxies found in clusters increases (Butcher & Oemler 1978; Aragón-Salamanca et al. 1993). A similar behavior has also been seen in these clusters using star formation tracers that are less sensitive to dust extinction, such as mid-infrared emission. Indeed, 24 μm surveys of actively star-forming galaxies using the MIPS instrument on the *Spitzer Space Telescope* have found increasing numbers of starbursts in clusters out to $z \sim 0.5$–1, although these clusters still typically contained a core of passive galaxies (e.g., Geach et al. 2006; Fadda et al. 2007; Saintonge et al. 2008; Haines et al. 2009; Finn et al. 2010; Biviano et al. 2011). The mass-normalized integrated star formation rate (SFR) for these systems increases with redshift as $\propto(1+z)^{\gamma}$ with $\gamma \sim 7$ (Geach et al. 2006), an accelerated evolution in comparison to the field where $\gamma \sim 4$ (Cowie et al. 2004).

Although these clusters are growing at $z \sim 0.5$–1, through the infall and accretion of star-forming galaxies from their environment, the cores still contain a population of massive, passive galaxies which suggests that at least some of their galaxies must have formed their stars at much earlier epochs. At higher redshifts, it has been shown that cluster cores show SFR densities equivalent to that of the field (Brodwin et al. 2013; Darvish et al. 2016), and in some $z \gtrsim 1$ cluster cores there are even claims of a reversal of the star-formation–density relation (e.g., Tran et al. 2010).

However, one issue with these studies is that for clusters at $z > 1$, the observed 24 μm emission, which is often used as a star formation tracer, becomes increasingly problematic due to the presence of strong, redshifted emission from polycyclic

aromatic hydrocarbon (PAH) and silicate absorption features that fall in the band. As a result, studies of more distant clusters have focused on the far-infrared/submillimeter wavebands and have uncovered evidence of a continued rise with redshift in the activity in overdense regions at $z > 1$, as traced by an increasing population of the most strongly star-forming, dusty (Ultra-)Luminous InfraRed Galaxies (U/LIRGs; e.g., Webb et al. 2005, 2013; Tran et al. 2010; Popesso et al. 2012; Smail et al. 2014; Noble et al. 2016). These studies have uncovered mixed evidence of a reversal in the star-formation–density relation in cluster cores at high redshift. For example, a "reversal" has been claimed in some massive clusters at $z \gtrsim 1.5$ such as XDCP J0044.0−2033 (Santos et al. 2015) and Cl J1001+0220 (Wang et al. 2016), but this is not ubiquitous. Smail et al. (2014) identify 31 probable cluster U/LIRGs within Cl J0218.3−0510 at $z = 1.62$. However, these highly star-forming galaxies did not reside in the densest regions of the cluster and instead the core was already populated with passive red galaxies, a trend also seen by Newman et al. (2014) in a $z = 1.8$ cluster, which has a cluster core dominated by a quiescent galaxy population. These results suggest that a massive quiescent population in some $z \sim 1.5$ cluster cores is already in place well before this epoch.

Some of the disagreement between the conclusions of these various studies may result from the uncertainties in reliably identifying the counterparts of far-infrared/submillimeter sources at other wavelengths, due to the typically poor spatial resolution of the long-wavelength data from single-dish facilities. To make progress on these issues, we took high-spatial resolution millimeter imaging of one of the well-studied high-redshift cluster which appears to exhibit a very significant overdensity of submillimeter sources in its core: XCS J2215.9−1738 (Stanford et al. 2006). This cluster has been claimed to exhibit enhanced star formation activity in its core regions (Hayashi et al. 2010), including a striking overdensity of submillimeter sources in single-dish 450/850 μm maps obtained by Ma et al. (2015).

In this paper, we present Atacama Large Millimeter/submillimeter Array (ALMA) interferometric observations of the dust continuum and CO emission of galaxies in the central region of XCS J2215. Our observations include a 1.2 mm mosaic of a 500 kpc diameter region encompassing the central four SCUBA-2 850 μm sources detected by Ma et al. (2015, hereafter Ma15). Our ALMA data provide us with the means to study the U/LIRG population in this cluster in the millimeter at resolutions an order of magnitude higher than that provided from current single-dish bolometer cameras and with much greater sensitivity. We use our ALMA continuum observations to robustly identify the 850 μm counterparts. We then searched for emission lines arising from molecular gas in cluster members. At the cluster redshift, our ALMA observations in Band 3 and Band 6 cover two transitions commonly seen in star-forming galaxies: ^{12}CO(2–1) and ^{12}CO(5–4). We employ these detections to confirm the cluster membership of U/LIRGs seen toward the cluster core and to estimate their molecular gas content and physical properties.

This paper is structured as follows: Section 2 covers the target selection, the ALMA observations, and data reduction, with the resultant continuum and CO line detections reported in Section 3. We then discuss these in Section 4 and give our main conclusions in Section 5. We assume a ΛCDM cosmology with $\Omega_M = 0.3$, $\Omega_\Lambda = 0.7$, and $H_0 = 70\,\mathrm{km\,s^{-1}\,Mpc^{-1}}$, which gives an angular scale of 8.5 kpc arcsec^{-1} at $z = 1.46$. We adopt a Chabrier initial mass function (IMF; Chabrier 2003), and any magnitudes are quoted in the AB system.

2. Observations and Data Reduction

2.1. XCS J2215.9–1738

XCS J2215 provides an excellent opportunity to study the nature of star formation activity in the central regions of a high-redshift cluster. At $z = 1.46$, it is one of the most distant clusters discovered in X-rays (Stanford et al. 2006) with extensive multiwavelength follow-up (Hilton et al. 2007, 2009, 2010; Hayashi et al. 2010, 2014). Of particular relevance here is the SCUBA-2 survey of the clusters by Ma15, which discovered an overdensity of submillimeter galaxies (SMGs) in its core. Unlike other (proto-)clusters studied at high redshifts (e.g., CLG J0218; Rudnick et al. 2012; Lotz et al. 2013; Hatch et al. 2016), XCS J2215 appears structurally well-developed. By combining *XMM-Newton* and *Chandra* observations, Hilton et al. (2010, hereafter H10) derived an X-ray luminosity of $L_X = 2.9^{+0.2}_{-0.4} \times 10^{44}\,\mathrm{erg\,s^{-1}}$ and an ICM temperature $T = 4.1^{+0.6}_{-0.9}$ keV. Employing the R_{200}–velocity dispersion relation of Carlberg et al. (1997; where R_{200} is the radius from the cluster center within which the mean density is 200 times the critical density at the redshift of the cluster), H10 used an iterative method to estimate a line-of-sight velocity dispersion of $\sigma_v = 720 \pm 110\,\mathrm{km\,s^{-1}}$ from the 31 galaxies with spectroscopic redshifts within $R_{200} = 0.8 \pm 0.1$ Mpc or 100″. The velocity distribution of the galaxies, however, did show signs of bimodality, suggesting that the cluster may not be a completely relaxed and virialized system.

Within the central 0.25 Mpc of the cluster, Hayashi et al. (2010, 2014) found 20 [O II] emitters with dust-free star formation rates (SFR) $> 2.6\,M_\odot\,\mathrm{yr^{-1}}$. Using *Spitzer*/MIPS, H10 found a further three bright 24-μm sources with estimated SFRs of $\sim 100\,M_\odot\,\mathrm{yr^{-1}}$ within the central 0.25 Mpc. However, as noted earlier, at $z = 1.46$, the broad PAH feature at 8.6 μm and potential silicate absorption features are redshifted into the 24 μm MIPS band, complicating the measurements of SFRs from this mid-infrared band. To provide a more robust census of luminous dusty galaxies, Ma15 obtained sensitive, longer wavelength observations of XCS J2215 with SCUBA-2 at 850/450 μm. These observations were combined with JVLA observations at 1.4 GHz and archival images and photometry from the *Hubble Space Telescope* (*HST*), Subaru, and *Spitzer* (respectively: Dawson et al. 2009; Hilton et al. 2009, 2010) to study the U/LIRGs in the cluster. Ma15 detected seven submillimeter sources above a 4σ significance cut within R_{200} (100″ radius), an order of magnitude above the expected blank-field counts. A further four fainter (>3σ) 850 μm sources were detected, which were confirmed through counterparts in *Herschel*/PACS 70 μm, 160 μm, and MIPS 24 μm. The probabilistic identification of counterparts to these submillimeter sources in the mid-IR and radio associated 9 of the 11 with galaxies that had spectroscopic or photometric redshifts that suggested they are cluster members. The total SFR from these potential U/LIRG cluster members yields an integrated SFR within R_{200} of $>1400\,M_\odot\,\mathrm{yr^{-1}}$; this suggests that XCS J2215 is one of the highest SFR clusters known at high redshifts (Ma et al. 2015).

We note that after the submission of this paper, Hayashi et al. (2017) published an ALMA Band 3 ^{12}CO(2-1) study of

XCS J2215. which overlaps with our observations. Their concentration on just ^{12}CO(2-1) enabled them to take deeper integrations over a slightly wider field and hence allowed them to detect fainter sources; however, where our observations overlap we obtain similar results.

2.2. ALMA Band 6 Observations

We obtained 1.25 mm continuum and simultaneous ^{12}CO($J = 5$–4) observations of the core of the XCS J2215 cluster using ALMA covering the core of the cluster, including four of the SCUBA-2 sources identified by Ma15. These Band 6 observations were carried out on 2016 June 19 (project ID: 2015.1.00575.S). To cover the ^{12}CO(5–4) emission lines, we set two spectral windows (SPWs) to cover the observed frequencies from 232.7 to 236.4 GHz or $\Delta V \sim 4800\,\mathrm{km\,s^{-1}}$, which comfortably covers the expected $720 \pm 110\,\mathrm{km\,s^{-1}}$ velocity dispersion of the cluster. A further two SPWs were centered at 248.9 and 251.4 GHz, where no visible emission lines are expected, for continuum imaging. Each SPW had a bandwidth of 1.875 GHz with a spectral resolution of 3.904 MHz for the emission-line SPWs (corresponding to a velocity resolution of 4.97–5.01 $\mathrm{km\,s^{-1}}$) and a spectral resolution of 31.250 MHz for the continuum SPWs (37.3–37.6 $\mathrm{km\,s^{-1}}$). At these frequencies, the FWHM of the primary beam is $\sim$25″; therefore, a mosaic of six pointings was required to map the central 500 kpc diameter covering the cluster core (Figure 1). The observations were conducted with forty-two 12 m antennae where the bandpass calibration was obtained from J2258−2758, the flux calibrator used was Titan, and the phase calibrator was J2206−1835 with an on-source integration time of 244 s for each pointing.

Calibration and imaging was carried out with the Common Astronomy Software Application (CASA v4.6.0; McMullin et al. 2007). The observation used a configuration that yielded a synthesized beam in Band 6 for the six pointings of $\sim$0.″66 × 0.″47 (PA $\sim$ 78°). The resulting continuum maps were created with the CLEAN algorithm using the multifrequency synthesis mode with a natural weighting to maximize sensitivity. We initially created a dirty image from the combined SPWs for each field and calculated the rms noise values. The fields are then initially cleaned to 3σ and then masking boxes are placed on sources >4σ and the sources cleaned to 1.5σ. The six fields were then combined to create a final image for source detection with an rms $\sigma_{1.25\,\mathrm{mm}} = 48\,\mu\mathrm{Jy\,beam^{-1}}$ at its deepest point, shown in Figure 1.

2.3. ALMA Band 3 Observations

As well as the Band 6 mosaic, we also obtained a single pointing in Band 3 centered on the cluster to cover ^{12}CO(2–1) emission from gas-rich cluster members. These observations were carried out on 2015 August 7 using thirty-nine 12 m antennae (project ID:2013.1.01213.S), using J2258−2758 as the bandpass calibrator, Ceres for the flux calibrations, and the phase calibrator was J2206−1835 with an on-science target integration time of 37.5 minutes. Two spectral windows were used, centered at observed frequencies 93.246 GHz and 95.121 GHz, with spectral bandwidths of 1.875 GHz and a resolution of 1.938 MHz for both SPWs (corresponding to 6.1–6.2 $\mathrm{km\,s^{-1}}$). At this observing frequency, the FWHM of the primary beam is $\sim$61″ and therefore the central $\sim$500 kpc of the cluster (Figure 1) could be covered in a single pointing. The same reduction approach was taken for the Band 3 observations as used for the Band 6 data, to create channel maps with a velocity resolution of 50 $\mathrm{km\,s^{-1}}$ and a noise level in each channel of 0.3–0.8 $\mathrm{mJy\,beam^{-1}}$.

2.4. Source Detection

To search for sources in the 1.25 mm continuum map, we used AEGEAN (Hancock et al. 2012) to identify >4σ detections. As part of this source extraction, we constructed a noise map for the mosaic by deriving standard deviations of the flux density in a box around each pixel with a size comparable to the synthesized beam. Bright pixels are rejected in each box using a 3σ clipping to avoid real sources contaminating the noise map. The outside edge of the ALMA mosaic was then trimmed to the half-width half-maximum radius of the primary beams, and source extraction was performed within this region which had a maximum noise of $\sigma_{\mathrm{rms}} = 0.09\,\mathrm{mJy\,beam^{-1}}$. Based on this noise map, we detect 14 S/N > 4.0σ candidate sources from the Band 6 continuum map shown in Figure 1 and listed in Table 1. All continuum sources have corresponding K_s, i_{850}, r_{775}, and H_{160} band counterparts within 0.″5 (Figures 1 and 2), and to estimate the reliability of these detections we perform the same detection routine in the negative source map, which yields zero detections at >4σ.

We compare this number of detections with the blank-field 1.2 mm number counts of from the Hubble Ultra Deep Field (Aravena et al. 2016; Dunlop et al. 2016; see also Oteo et al. 2016). For sources brighter than a flux limit of $\sim$0.18 mJy, we would expect $\sim 2 \pm 1$ sources in the area of our continuum map. Therefore, we appear to be detecting a $\sim$7× overdensity of millimeter sources in the central projected 500 kpc of XCS J2215 seen in Figure 1.

To search for ^{12}CO emission lines, we first adopted a targeted search by extracting spectra from the Band 3 and 6 datacubes at the positions of the fourteen 1.25 mm continuum detections. In addition, we extract spectra at the positions of the 25 spectroscopic members from H10, the 46 sources from H09 with photometric redshifts indicating possible cluster membership, and the 20 [O II] emitters from Hayashi et al. (2014) that are within the footprint of the ALMA observations.

We detect six significant emission lines in the Band 3 data, all corresponding to bright dust continuum sources (IDs: 3, 6, 7, 8, 11, and 12 in Figure 1). One of these sources, ID 6, also has a redshift from H10: $z = 1.454$, consistent with our ^{12}CO-derived measurement; Hayashi et al. (2017) also report ^{12}CO(2–1) detections for all six of these sources with redshifts consistent with our own. We identify all of these lines as ^{12}CO(2–1) from cluster members and plot the spectra for these in Figure 3. Applying the same procedure on the Band 6 cube yielded significant detections of ^{12}CO(5–4) from just the same six sources; these are also shown in Figure 3 and the line emission is contoured over the continuum in Figure 2 showing that the high-J gas is collocated with the rest-frame 500 μm dust emission. For the ^{12}CO(5–4) emission lines, we subtracted the continuum emission in the uv data using the UVCONSTSUB task in CASA and, by averaging the data across channels, created continuum-subtracted channel maps at a velocity resolution of 50 $\mathrm{km\,s^{-1}}$ with an rms of 0.3–0.4 $\mathrm{mJy\,beam^{-1}}$. We find no individually detected ^{12}CO(2–1) or ^{12}CO(5–4) emission from any of the other sources in the spectroscopic or photometric samples.

For the galaxies where ^{12}CO emission lines were detected, we calculated the intensity-weighted redshift. This was

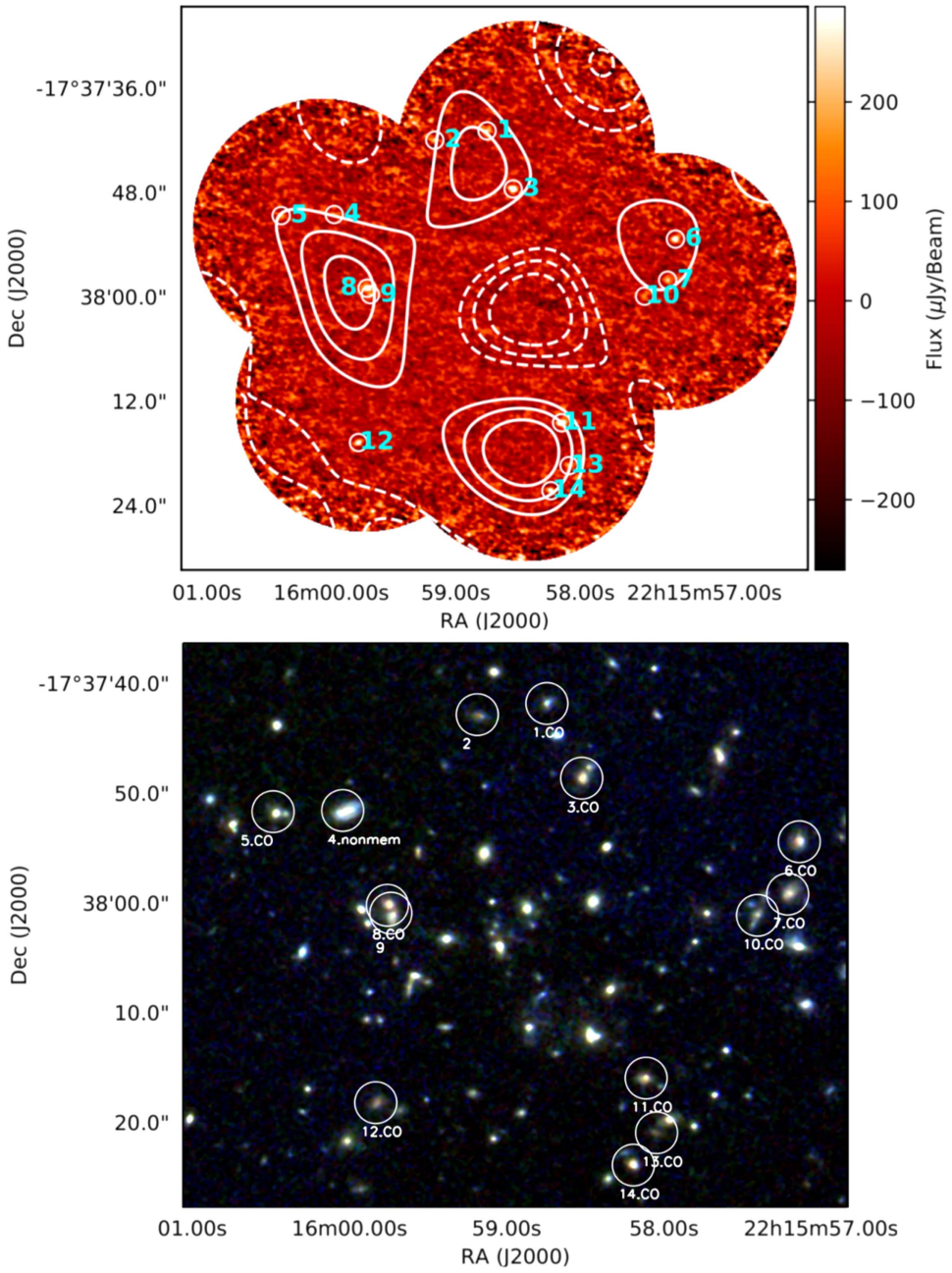

Figure 1. Upper panel: the ALMA 1.25 mm (Band 6) mosaic of XCS J2215 taken from six overlapping pointings covering a 500 kpc diameter region in the cluster core. We detect 14 $> 4\sigma$ continuum detections, demonstrating a very significant overdensity of millimeter sources in this region marked by circles and numbered. We list their properties in Table 1. We also overlay the SCUBA-2 850 μm S/N contours from Ma15 starting at 2σ and increasing in steps of 1σ (dashed lines showing the equivalent negative contours). Lower panel: a slightly zoomed three-color *HST* image (F125W, F140W, and F160W), with our ALMA detections labelled, showing the rest-frame *V*-band morphologies of the millimeter sources. We highlight source #4 as "nonmem" as this is a known interloper from its spectroscopic redshift; all other sources have either ^{12}CO (labelled "CO") detections from this study or archival ^{12}CO(2–1), which confirm cluster membership (11 sources) or photometric redshifts suggesting possible membership (IDs 2, 9).

calculated for both the ^{12}CO(5–4) and ^{12}CO(2–1) lines, and for both lines for all six sources, the derived redshifts were in excellent agreement, as can be seen in Figure 3. The redshift values reported in Table 2 are the means of the redshifts derived from the two transitions. Line widths are derived from fitting Gaussian profiles to the binned spectra using scipy.curve_fit in PYTHON weighted by the uncertainty in the spectra.

We attempted a blind search for CO emission lines in the Band 3 and 6 cubes by collapsing them in 300 km s^{-1} wide bins (similar to the observed FWHM of the targeted detections) and stepping the bins in 100 km s^{-1} increments across a velocity range $-2\sigma_v < v < +2\sigma_v$, where σ was the given velocity dispersion of the cluster from H10. AEGEAN was used to detect peaks in these collapsed channel maps, looking for $>4\sigma$ detections. This procedure recovered the six previously identified line emitters but did not uncover any additional blind detections. We do see hints ($<3.5\sigma$) of further ^{12}CO(5–4) detections at the locations and redshifts of two of the ^{12}CO(2–1) detections from Hayashi et al. (2017; ALMA.B3.04 and ALMA.B3.08); however, these are all faint and none

Table 1
Properties of the ALMA 1.25 mm Continuum Detections in XCS J2215

ID	R.A. (J2000)	Decl.	$S_{1.25\,mm}$ (mJy)	L_{FIR} (10^{11} $L_{\odot}$)	SFR ($M_{\odot}$ yr^{-1})	z_p (H09)	z_s[a]	
1	22 15 58.75	−17 37 40.9	0.46 ± 0.09	$3.5^{+1.9}_{-2.2}$	50^{+30}_{-30}	$1.44^{+1.10}_{-1.10}$	1.451[b]	1.451 (1.464)[c]
2	22 15 59.17	−17 37 41.9	0.49 ± 0.08	$2.8^{+1.3}_{-1.4}$	40^{+20}_{-20}	$1.15^{+2.80}_{-0.20}$	...	...
3	22 15 58.54	−17 37 47.6	0.93 ± 0.05	$8.8^{+4.4}_{-2.2}$	130^{+60}_{-30}	$1.99^{+0.39}_{-0.57}$	**1.453**	1.454
4	22 15 59.98	−17 37 50.5	0.21 ± 0.04	$3.6^{+2.1}_{-1.2}$	50^{+30}_{-20}	$1.25^{+0.11}_{-0.36}$	*1.301*	1.302
5	22 16 00.40	−17 37 50.6	0.37 ± 0.07	$1.7^{+0.6}_{-0.8}$	20^{+10}_{-10}	$1.33^{+0.69}_{-0.19}$	1.451[b]	1.452
6	22 15 57.23	−17 37 53.3	0.68 ± 0.08	$9.4^{+2.7}_{-1.7}$	140^{+40}_{-30}	$1.30^{+0.92}_{-0.48}$	**1.454**	1.454
7	22 15 57.30	−17 37 58.0	0.46 ± 0.09	$3.6^{+1.9}_{-2.0}$	50^{+30}_{-30}	$1.35^{+1.00}_{-0.18}$	**1.450**	1.453
8	22 15 59.71	−17 37 59.0	0.88 ± 0.08	$3.3^{+0.9}_{-1.1}$	50^{+10}_{-20}	$1.32^{+1.10}_{-0.35}$	**1.466**	1.468
9	22 15 59.69	−17 37 59.7	0.28 ± 0.05	$6.7^{+2.5}_{-1.7}$	100^{+40}_{-20}	$1.50^{+0.81}_{-0.22}$	...	...
10	22 15 57.48	−17 37 59.9	0.18 ± 0.04	$1.8^{+0.8}_{-1.3}$	30^{+10}_{-20}	$1.97^{+0.37}_{-0.61}$	1.450[b]	1.451
11	22 15 58.15	−17 38 14.5	0.98 ± 0.06	$5.5^{+1.6}_{-2.8}$	80^{+20}_{-40}	$1.73^{+0.52}_{-0.36}$	**1.467**	1.467
12	22 15 59.78	−17 38 16.7	0.60 ± 0.09	$2.4^{+1.4}_{-1.0}$	40^{+20}_{-10}	$1.54^{+0.86}_{-0.47}$	**1.472**	1.472
13	22 15 58.09	−17 38 19.4	0.30 ± 0.07	$3.9^{+1.2}_{-0.6}$	60^{+20}_{-10}	$1.34^{+1.70}_{-0.66}$	1.467[b]	1.469
14	22 15 58.23	−17 38 22.3	0.56 ± 0.08	$3.6^{+2.0}_{-1.9}$	50^{+30}_{-30}	$1.46^{+0.99}_{-0.32}$	1.457[b]	1.457

Notes.
[a] Spectroscopic redshifts in bold are from ^{12}CO emission described in this paper; confirmed non-members are in italics.
[b] ^{12}CO spectroscopic redshifts from Hayashi et al. (2017).
[c] There are two galaxies separated by <0.″5 and ∼1500 km s^{-1}, both of which are detected in CO and [O II].

of them make our selection cut and so they are not considered in the rest of the paper.

2.5. MUSE AO Observations

Observations of the central 1 × 1 arcmin of XCS J2215 were taken with the MUSE IFU during the science verification of the wide-field adaptive optics (WFM-AO) mode on 2017 August 15. In this mode, the GALACSI AO system is used to increase the Strehl ratio of the observations by employing four laser guide stars (and a deformable secondary mirror) to correct for the turbulent atmospheric ground layer. An $R = 16.1$ mag star located 95″ from the field center was used to correct for the remaining atmospheric tip-tilt. In total, we observed the cluster core for 3.5 ks, which was split into four 860 s exposures, each of which was spatially dithered by ∼5″. Between exposures, the IFU was also rotated through 90° to improve the flat-fielding along slices in the final datacube. We used the standard spectral range, which covers 4770–9300 Å and has a spectral resolution of $R = \lambda/\Delta\lambda = 4000$ at $\lambda = 9200$ Å (the wavelength of [O II] at the redshift of the cluster sample)—sufficient to resolve the [O II]λλ3726.2,3728.9 emission-line doublet.

To reduce the data, we use the MUSE ESOREX pipeline which extracts, wavelength-calibrates, flat-fields the spectra, and forms each datacube. Each observation was interspersed with a flat-field to improve the slice-by-slice flat-field (illumination) effects. Sky subtraction was performed on each sub-exposure by identifying and subtracting the sky emission using blank areas of sky at each wavelength slice, and the final mosaics were then constructed using an average with a 3σ clip to reject cosmic rays, using point sources in each (wavelength collapsed) image to register the cubes.

For each source in our 1.2 mm catalog, we extract a spectrum by integrating the datacube within a 0.″5 aperture and search for the [O II] emission at the cluster redshift. For all of the galaxies with CO detections, we detect the [O II] emission line with signal-to-noise ratio ranging from 5 to 100. We fit the [O II] emission doublet and derive redshifts that agree with the CO (within their 1σ error) in all cases. We report the [O II] emission-line redshifts in Table 1.

3. Analysis and Results

Our ALMA survey of the central regions of XCS J2215 has resolved the overdensity of four submillimeter sources in the core of the cluster into 14 separate 1.25 mm continuum sources (Figure 1). The four brightest 1.25 mm continuum components each correspond to one of the SCUBA-2 sources discovered by Ma15: our ID 11 corresponds to SCUBA-2 source #4 from Ma15, ID 3 is #11, ID 8 is #6, and ID 6 is #13. Our ALMA-detected millimeter sources also confirm the primary IDs proposed by Ma15 for these single-dish sources, but their analysis did not identify any of the other 10 sources detected by ALMA in this region, which contribute to the sub/millimeter flux seen by SCUBA-2.

As noted above, the five brightest millimeter continuum sources (plus the seventh) also exhibit ^{12}CO(2–1) and ^{12}CO(5–4) emission with redshifts that place them within the cluster. In addition, we match the remaining fainter continuum sources to the Hayashi et al. (2017) ^{12}CO(2–1) catalog, finding five further matches: IDs 1, 5, 10, 13, and 14. Matching to the H10 redshift catalog finds that a further continuum source, ID 4, has a spectroscopic redshift of $z = 1.301$, making it an interloper in the foreground of the cluster, and we do not consider it a cluster member in the following analysis. In the remaining two continuum-selected ALMA sources (ID 2 and 9), we do not detect any emission lines in the MUSE spectra, which covers 4770–9300 Å (which corresponds to $z = 0.28$–1.50 for [O II] emission). However, we note that both of these two galaxies in the H09 photometric redshift catalog have redshifts that are consistent with being possible cluster members, although the absence of lines in the MUSE spectra either suggests that they are highly obscured or they lie at higher redshift than $z = 1.50$. For the 11 spectroscopically confirmed millimeter-selected cluster members, we derive a rest-frame velocity dispersion of $\sigma = 1040 \pm 100$ km s^{-1}. This

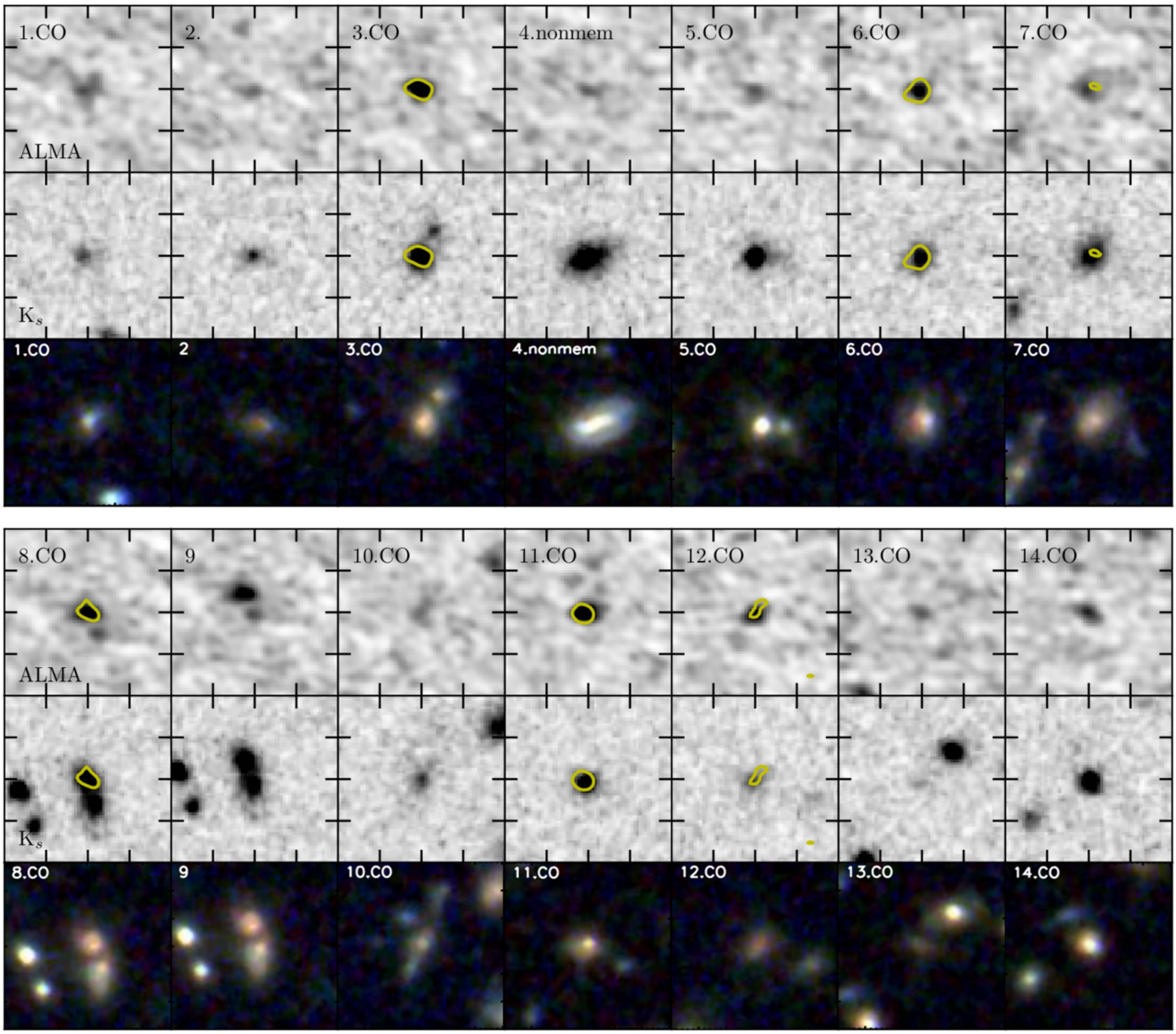

Figure 2. Thumbnails showing the ALMA Band 6 continuum (top row of each panel), K_s (middle row of each panel), and three-color *HST* WFC3 images (1.25, 1.40, and 1.60 μm, lower row of each panel) of the S/N > 4 millimeter continuum sources detected in our map. Several sources display disturbed morphologies or very close neighbors (although these are typically faint in K_s and hence likely to be low mass), suggesting that dynamical interactions may be triggering the strong star formation in these galaxies. Each of these thumbnails is centered on the positions given in Table 1. Six of the brightest sources in the ALMA continuum map: IDs 3, 6, 7, 8, 11, and 12 additionally yield ^{12}CO(2–1) and ^{12}CO(5–4) emission-line detections, while IDs 1, 5, 10, 13, and 15 have archival ^{12}CO(2–1) detections from Hayashi et al. (2017), confirming that these are members of the cluster. Each thumbnail is $6'' \times 6''$ with major ticks every $1\overset{''}{.}5$ and with north up and east left. The yellow contours show the 3σ contour for the integrated ^{12}CO(5–4) map across the FWHM of the detected lines, showing that the high-J ^{12}CO emission is aligned with the dust continuum.

is marginally higher than the $\sigma = 720 \pm 110\,\mathrm{km\,s^{-1}}$ determined by H10 for the cluster members within the cluster core. This difference is not statistically significant ($\sim 2\sigma$), but the sense of the difference is consistent with the expectation that the millimeter-selected sources are likely to be relatively recently accreted galaxies which have yet to fully virialize.

Our ALMA observations provide precise positions for the sub/millimeter emission and so unambiguously identify the counterparts in the optical and near-infrared wavebands, as shown in Figures 1 and 2. Over half of these sources have companions on scales of $\sim 2''$–$3''$, although more than half of these are faint or undetected in the K_s band, suggesting that they have relatively modest stellar masses. Nevertheless, this is some indication that close tidal interactions or minor mergers may be the trigger for the starburst activity seen in this population.

3.1. SED Fitting

We estimate the far-infrared luminosities for each of our continuum sources by fitting their far-infrared and submillimeter photometry using a library of galaxy template SEDs from

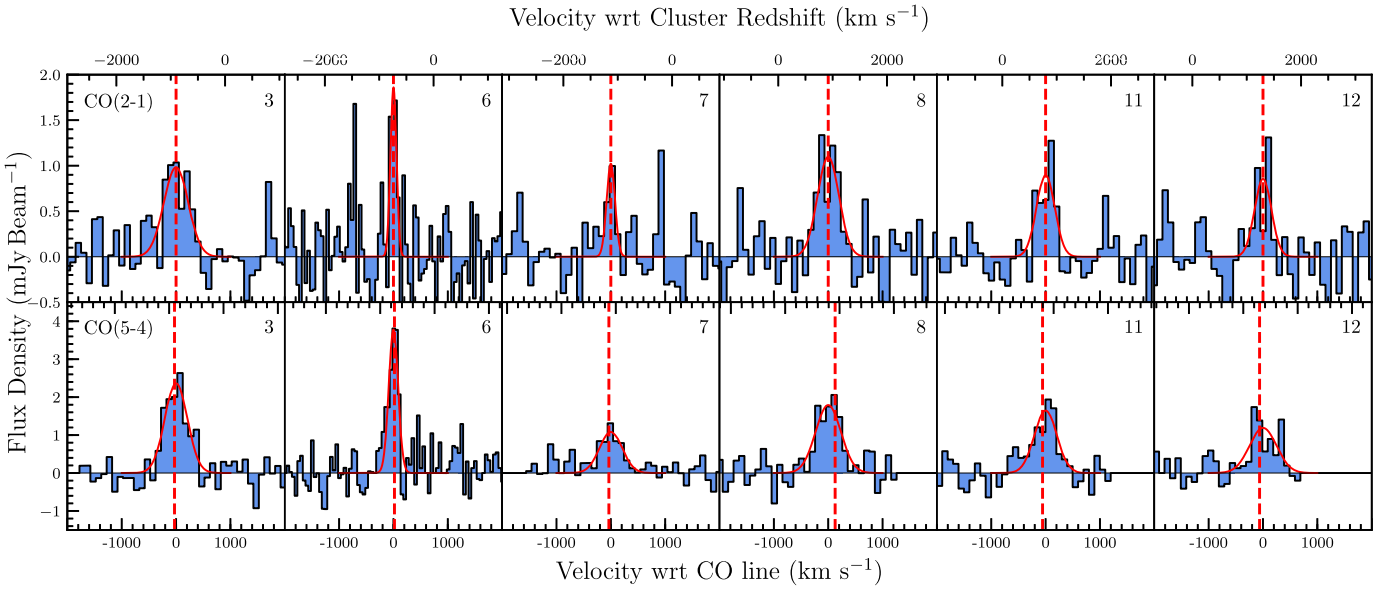

Figure 3. Spectra of the six ^{12}CO-detected cluster members with the top row showing the ^{12}CO(2–1) emission in Band 3 and the bottom row the ^{12}CO(5–4) lines that fall in Band 6. In each case, the best-fitting single-Gaussian profiles are overlaid. We see detections of lines in both transitions in all six sources, confirming these millimeter sources as gas-rich cluster members. The lower velocity axis is centered on the peak velocity of the Gaussian fit to the ^{12}CO(2–1) line, while the upper velocity axis shows a velocity scale relative to the nominal cluster redshift of $z = 1.460$. The spectra for IDs 3, 7, 8, 11, and 12 are binned to 100 km s^{-1} resolution; however, for ID 6 the data were binned at 50 km s^{-1} due to their narrow line width. The lack of spectral coverage at velocities >1000 km s^{-1} for ^{12}CO(5–4) IDs 8, 11, and 12 is due to the edge of the spectral window. The dashed red vertical lines show the velocity at which the ^{12}CO(2–1) Gaussians peak for each of our six detections.

Chary & Elbaz (2001), Draine et al. (2007), and Rieke et al. (2009). We use our 1.25 mm continuum fluxes along with fluxes from the lower resolution single-dish observations from SCUBA-2 at 450 and 850 μm (Ma et al. 2015) and archival *Herschel* PACS data at 100 and 160 μm (see Santos et al. 2013). Due to the low resolution for the single-dish observations, the fluxes for the individual sources were estimated by deblending these maps using the method detailed in Swinbank et al. (2013) using the ALMA detections as positional priors as described in Ma15. We calculate the infrared luminosity from integrating the best-fitting SEDs for each galaxy in the wavelength range 8–1000 μm, and from this derived the far-infrared luminosity assuming the sources lie at the cluster redshift (Table 1). The far-infrared luminosities show a ∼50% dispersion at a fixed 1.25 mm flux, but the formal error bars are consistent with a single ratio, and hence there is no strong evidence for a variation in the SED shape within our small sample. In particular, we note that we obtained ^{12}CO detections for the six brightest 1.25 mm continuum sources, only three of which fall in the top five brightest sources based on the far-infrared luminosities. This may indicate that the far-infrared luminosities may be less reliable than adopting a single representative SED model and fitting this just to the 1.25 mm continuum flux. We also caution that if there are systematic differences in the dust SEDs of galaxies in high-density environments, e.g., due to stripping of diffuse cold gas and dust components (Rawle et al. 2012), then this will not be captured by the templates in our library.

We next estimate the SFR from the far-infrared luminosities using the Kennicutt (1998) relation and assuming a Chabrier IMF. For the 14 ALMA continuum sources, we derive $L_{\rm IR}$ in the range of $(1.7–9.1) \times 10^{11}\,L_{\odot}$ and a median $(3.6^{+2.1}_{-1.2}) \times 10^{11}\,L_{\odot}$, which corresponds to SFRs of ∼20–140 $M_{\odot}\,{\rm yr}^{-1}$ (Table 1). The derived luminosities of $L_{\rm IR} = 10^{11}$–$10^{12}\,L_{\odot}$ classify these cluster galaxies as LIRGs, with the brightest on the ULIRG boundary.

Integrating the ongoing star formation in the spectroscopically confirmed millimeter-selected cluster members, we derive a total SFR in the central ∼500 kpc of the cluster of $\gtrsim$700 $M_{\odot}\,{\rm yr}^{-1}$. Including the photometrically identified members (but excluding ID 4), this increases to $\gtrsim$840 $M_{\odot}\,{\rm yr}^{-1}$. This is comparable to the total SFR estimated by Ma15 within $R_{200} = 0.8$ Mpc (∼100″), even though that region is much larger than the extent of our current ALMA survey of the central $R \leqslant 0.25$ Mpc (Figure 1). Thus, our results reinforces the claims that XCS J2215 demonstrates a very rapid increase in the SFR density in the central regions of clusters out to $z \sim 1.5$ and beyond.

3.2. CO Line Properties

To derive ^{12}CO line properties, we fit single Gaussians to each of the Band 3 and 6 emission spectra, which appear to provide adequate descriptions of the observed line profiles (Figure 3). Estimates of the line widths were taken from the FWHM of the Gaussian fits, and the flux density of the ^{12}CO lines were determined by integrating the ^{12}CO spectrum,

$$I_{\rm CO} = \int_{-2\sigma}^{+2\sigma} I(v)dv, \qquad (1)$$

where σ was taken from the Gaussian fits. Then, the ^{12}CO luminosities were calculated using the relation given in Solomon & Vanden Bout (2005),

$$L'_{\rm CO} = 3.25 \times 10^7 S_{\rm CO}\Delta v \nu_{\rm obs}^{-2} D_L^2 (1+z)^{-3}, \qquad (2)$$

where $L'_{\rm CO}$ is the line luminosity in K km s^{-1} pc^2, $S_{\rm CO}\Delta v$ is the observed velocity-integrated flux density in Jy km s^{-1}, ν is the observed frequency of the emission line in GHz, and D_L is the luminosity distance in Mpc. The FWHM and ^{12}CO flux densities for both transitions are given in Table 2. For simplicity in comparing to the literature, we adopted the same

Table 2
Emission-line Properties for ^{12}CO(2–1) and ^{12}CO(5–4) Detections in XCS J2215 Member Galaxies

ID	$I_{CO(2-1)}$ (J km s^{-1})	FWHM$_{CO(2-1)}$ (km s^{-1})	$I_{CO(5-4)}$ (J km s^{-1})	FWHM$_{CO(5-4)}$ (km s^{-1})	M_{gas} (10^{10} $M_{\odot}$)	M_{dyn} (10^{10} $M_{\odot}$)
3	0.5 ± 0.1	530 ± 90	1.2 ± 0.1	490 ± 40	2.4 ± 0.7	11 ± 4
6	0.25 ± 0.08	130 ± 30	0.80 ± 0.09	200 ± 20	1.0 ± 0.2	0.6 ± 0.3
7	0.19 ± 0.09	190 ± 120	0.6 ± 0.1	490 ± 60	1.3 ± 0.2	9 ± 5
8	0.6 ± 0.1	460 ± 90	1.0 ± 0.1	550 ± 50	2.2 ± 0.6	9 ± 4
11	0.4 ± 0.1	390 ± 90	0.8 ± 0.1	490 ± 50	1.6 ± 0.5	6 ± 3
12	0.3 ± 0.1	370 ± 90	0.7 ± 0.2	580 ± 100	1.5 ± 0.7	5 ± 3

values for the constants $\alpha_{CO} = 1$, radius of galaxy $R_{kpc} = 7$ kpc, and the $L_{CO(2-1)}/L_{CO(2-1)}$ ratio of 0.84 ± 0.13 from Bothwell et al. (2013) when deriving M_{gas} and M_{dyn}. We then list the estimated gas masses (M_{gas}) for the galaxies based on their ^{12}CO(2–1) luminosities and adopting $\alpha_{CO} = 1$ (following Bothwell et al. 2013). We also list the dynamical masses (M_{dyn}) for a disk-like dynamical model with a 7 kpc radius and the average inclination for a population of randomly oriented disks (again following Bothwell et al. 2013). We note that the derived values are highly dependent on the value of α_{CO}, and due to the SFRs being lower than the ULIRG sources in Bothwell et al. (2013), a more Milky Way-like $\alpha_{CO} \sim 4.4$, which has been claimed to be appropriate for less active high-redshift galaxy populations, might be more applicable (Tacconi et al. 2013); however, a Milky Way-like α_{CO} results in gas masses for two out of our six detections being greater than our calculated dynamical masses. We note that our dynamical masses, while consistent with the independent stellar mass estimations shown below, are based on adopting a mean inclination angle for populations of randomly oriented disks and an adopted value for the galaxy radius of $R_{kpc} = 7$ kpc. However, the two galaxies with gas fractions >1 adopting $\alpha_{CO} \sim 4.4$ are ID 6 and ID 7 (see Figure 2), and from their *HST* morphologies they do not appear "edge-on;" therefore, the inclination angle assumption will not create an underestimation of their dynamical masses. To reconcile the unphysical gas fractions would require dynamical masses estimated with galaxies of radii >35 kpc, which is again unphysical and an order of magnitude greater than previous size estimators of ^{12}CO-emitting regions (Engel et al. 2010). This suggests, that for at least these two galaxies, a Milky Way-like $\alpha_{CO} \sim 4.4$ is an inappropriate conversion factor to use and a lower value more typical for local ULIRGs is more appropriate.

The median gas mass for the six galaxies is $M_{gas} = 1.6 \pm 0.2 \times 10^{10}$ $M_{\odot}$ (or $M_{gas} = 4.3$–10.5×10^{10} $M_{\odot}$ for $\alpha_{CO} = 4.36$), the median dynamical mass is $M_{dyn} = 0.9^{+0.3}_{-0.6} \times 10^{10}$ R_{kpc} $M_{\odot}$ ($M_{dyn} = 6^{+2}_{-4} \times 10^{10}$ $M_{\odot}$ for $R_{kpc} = 7$ kpc), and the median gas fraction is relatively low at $f_{gas} = 0.3 \pm 0.3$. We estimate stellar masses for our 1.2 mm continuum-selected galaxies using their *Spitzer* imaging. In particular, we exploit the archival IRAC imaging of XCS J2215 to measure IRAC 3.6 μm magnitudes for our sources, deriving a median magnitude of $21.1^{+0.1}_{-0.2}$. At $z = 1.45$, this corresponds to the rest-frame *H*-band, which is sensitive to the underlying stellar mass of a galaxy. We exploit the MAGPHYS-derived stellar masses of comparably luminous submillimeter-selected galaxies in the Extended *Chandra* Deep Field South from da Cunha et al. (2015) and apply their median rest-frame *H*-band mass-to-light ratio to our sample. We derive a median stellar mass of $M_* = 4^{+2}_{-2} \times 10^{10}$ $M_{\odot}$, which suggests a median gas fraction for our six sources with CO detections of $f_{gas} = 0.3 \pm 0.4$ for $\alpha_{CO} = 1.0$, which is in excellent agreement with the gas fractions derived from the dynamical masses, suggesting our choice of $R_{kpc} = 7$ kpc is appropriate.

Combining these gas masses with the SFRs, we estimate a median gas consumption timescale of 200 ± 100 Myr, which is comparable to the crossing time of the cluster core. However, as noted above, this is highly dependent on the choice of α_{CO}, scaling linearly; therefore, if a more Milky Way-like α_{CO} is appropriate, then the consumption timescale increases to ~800 Myr, which is comparable to timescales expected for similar main-sequence galaxies at this redshift (~1.1 ± 0.2 Gyr, Genzel et al. 2015). We note that the fainter ^{12}CO detections for the remaining millimeter sources with archival ^{12}CO detections indicate gas masses of $\lesssim 1 \times 10^{10}$ $M_{\odot}$, and this may reduce the median gas consumption timescale for the whole population (although these fainter members also tend to have lower SFRs; Table 1).

For the two continuum sources without spectroscopic redshifts, from their calculated L_{IR} and based on the scatter in the L'_{CO}–L_{IR} relation shown in Figure 5, it is plausible that we might not detect ^{12}CO(5–4) for ID 9. For ID 2, on the other hand, the combination of its faint continuum detection and location close to the edge of the ALMA primary beam (see Figure 1) points to a non-detection possibly being a result of insufficient sensitivity.

As we have observations of two ^{12}CO transitions for our ALMA-identified cluster U/LIRGs, we can determine the ratio of the line brightness temperatures between the ^{12}CO(5–4) and ^{12}CO(2–1) transitions. We show in Figure 4 the spectral line distributions (SLEDs) for our sources compared to other populations and models from the literature. This shows that the cool interstellar medium within our cluster LIRGs is less excited than comparably luminous local galaxies, although it has very similar properties to that seen in high-redshift, submillimeter-selected ULIRGs and *BzK* galaxies. To quantify this further, we determine a median value of the ^{12}CO(5–4) and ^{12}CO(2–1) line brightness ratio for our six sources of $r_{54/21} = 0.37 \pm 0.06$. We can compare this to the value derived for statistical samples of high-redshift, submillimeter-selected ULIRGs from (Bothwell et al. 2013) and *BzK*s from Daddi et al. (2015): $r_{54/10} = 0.32 \pm 0.05$ and $r_{21/10} = 0.84 \pm 0.13$, which yield $r_{54/21} = 0.38 \pm 0.08$ for SMGs and $r_{54/10} = 0.23 \pm 0.04$ and $r_{21/10} = 0.76 \pm 0.09$, which yield $r_{54/21} = 0.32 \pm 0.06$ for *BzK*s. As expected from Figure 4, these are in agreement to the values we derive and suggests comparable gas excitation in our sample of $z = 1.46$ cluster LIRGs to the more luminous and typically higher-redshift field

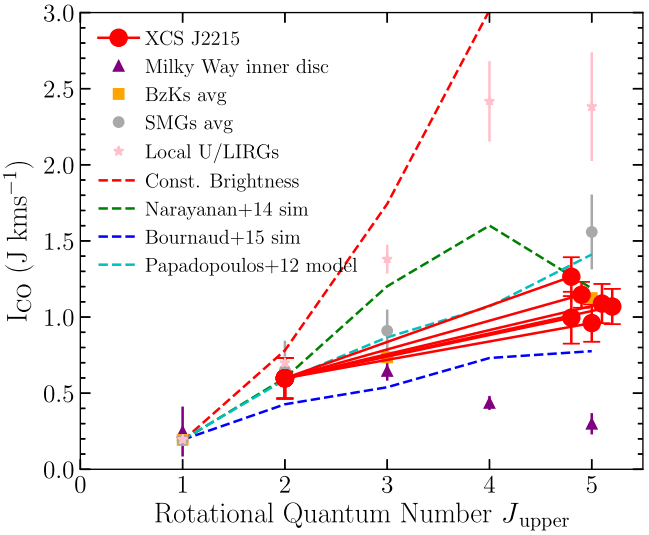

Figure 4. ^{12}CO SLEDs for the six XCS J2215 LIRGs compared to SLEDs for other populations from the compilation of Daddi et al. (2015). We see that our cluster LIRGs have SLEDs that peak at higher-J than the Milky Way (Fixsen et al. 1999), indicating that the interstellar medium in these galaxies is more excited, although less excited than that in local U/LIRGs (Papadopoulos et al. 2012). Our sources appear to be similar to the submillimeter-selected field ULIRGs studied by Bothwell et al. (2013) and to the less luminous *BzK*s from Daddi et al. (2015). We also show model SLEDs from the simulations of Narayanan et al. (2012) and Bournaud et al. (2015), and the toy model of Papadopoulos et al. (2012). The latter implies that the interstellar medium is a two-phase mix of star-forming and non-star-forming gas, with 10% of its gas in the star-forming phase. All of the SLEDs are normalized to the average $J = 1$ transition for the Daddi et al. (2015) *BzK* average, except for the Milky Way and XCS J2215 SLEDs, which are normalized to the *BzK* average $J = 2$ transition. We note that if environmental processing has preferentially removed cool material from these galaxies, then their measured SLED will appear to be more "active" than it initially started off with.

SMGs studied by Bothwell et al. (2013), as well as the less luminous *BzK*s. This in turn suggests that the $r_{21/10}$ values for the Bothwell et al. (2013) sample should be broadly applicable to our sources.

4. Discussion

Our high-resolution continuum observations with ALMA confirmed and significantly expanded the overdensity of luminous, dusty star-forming galaxies known in XCS J2215. Our data also enable us to survey the cluster for massive gas reservoirs, and we find six gas-rich systems, associated with the typically brighter dust continuum sources. These ^{12}CO detections, along with five sources that have archival ^{12}CO detections, unambiguously demonstrate that the majority of these galaxies are members of the cluster, while photometric redshifts suggest that two of the remaining continuum sources are also possible members.

We can use the CO line properties for our sources to compare to similar observations of other galaxy populations at high and low redshifts to understand their physical properties. Hence, while L'_{CO} provides a tracer for the molecular gas content in these galaxies, the FWHM of the emission lines provides us with a degenerate tracer of both the dynamical mass of the galaxy (narrower FWHM suggests lower mass) and inclination of the galaxy (narrower FWHM suggests a more "face-on" galaxy). In Figure 5(a), we compare $L'_{CO(1-0)}$ (converted from our $L'_{CO(2-1)}$ detections, adopting $r_{21/10} = 0.84$) versus FWHM for our six ^{12}CO-detected galaxies against a sample of local and high-redshift U/LIRGs. As in Bothwell et al. (2013), we overlay the functional form given in Equation (3),

$$L'_{CO(1-0)} = \frac{(V/2.35)^2 R}{1.36 \alpha G}, \quad (3)$$

where V is the FWHM of the line, 1.36α is the ^{12}CO to gas mass conversion factor, R is the radius of the ^{12}CO(2–1) emission region, and G is the gravitational constant. We, again, adopt the values of $\alpha = 1$ and $R = 7$ kpc (Bothwell et al. 2013). We see that LIRGs identified with ALMA in XCS J2215 fall within the scatter of the properties of local U/LIRGs, but slightly below the *BzK*s population seen at similar redshifts. They may also show a marginally shallower trend than the functional form given in Equation (3), although the latter provides a good fit for the higher redshift and higher luminosity SMGs in Bothwell et al. (2013). We stress that the conversion of the line luminosities to ^{12}CO(1–0) may result in systematic uncertainties between samples and individual sources in Figure 5.

Comparing the line widths for the ^{12}CO(2–1) and ^{12}CO(5–4) emission lines for individual galaxies in our sample, we derive a median ratio of $\mathrm{FWHM}_{21}/\mathrm{FWHM}_{54} = 0.7 \pm 0.2$. If both transitions are tracing the rising part of the rotation curve in these galaxies, this marginal difference suggests that the ^{12}CO(5–4) emission may be more extended than ^{12}CO(2–1). This is the opposite behavior to that expected if transitions with lower excitation temperatures have larger contributions from cool gas on the outskirts of galaxies (Papadopoulos et al. 2001; Ivison et al. 2011; Bolatto et al. 2013). This could reflect environmental influences on the gas disks in these cluster LIRGs, with the removal of the more diffuse cool interstellar medium from their extended disks. Similar environmentally driven stripping of cooler material was invoked by Rawle et al. (2012) to explain the apparently higher dust temperatures seen in the SEDs of star-forming galaxies in $z \sim 0.3$ clusters. We note that this would imply that before material was removed, the galaxies would have had a lower $r_{54/21}$ ratio than is currently observed, implying that originally they had a lower excitation SLED and a higher cold gas and dust mass and gas fraction.

As the far-infrared luminosity traces a galaxy's SFR and L'_{CO} traces its gas content, we show the ratio of these two observables for the ALMA-detected population in XCS J2215 in comparison to similar galaxies in the low- and high-redshift field in Figure 5(b). To try to limit the effect of potential systematic errors, we plot the line luminosities derived directly from our higher-S/N ^{12}CO(5–4) detections, $L'_{CO(5-4)}$, and compare to similar high-J observations of the other populations (following Daddi et al. 2015). Again, we see that our sources lie within the scatter of the local U/LIRG population, although they lie on the high side of the distribution. In comparison to the linear fit of the local U/LIRG population, our cluster galaxies show a median increase in $L'_{CO(5-4)}$ for their detected L_{IR} of 48% ± 12% (or conversely a deficit in L_{IR} at a fixed $L'_{CO(5-4)}$). One possible explanation for this trend would be if the far-infrared luminosities of these sources are underestimated due to a relative paucity of cold dust (a consequence of the estimates of their far-infrared luminosities being driven primarily by the 1.25 mm flux measurements due to their comparatively small errors in the SED fitting), due to

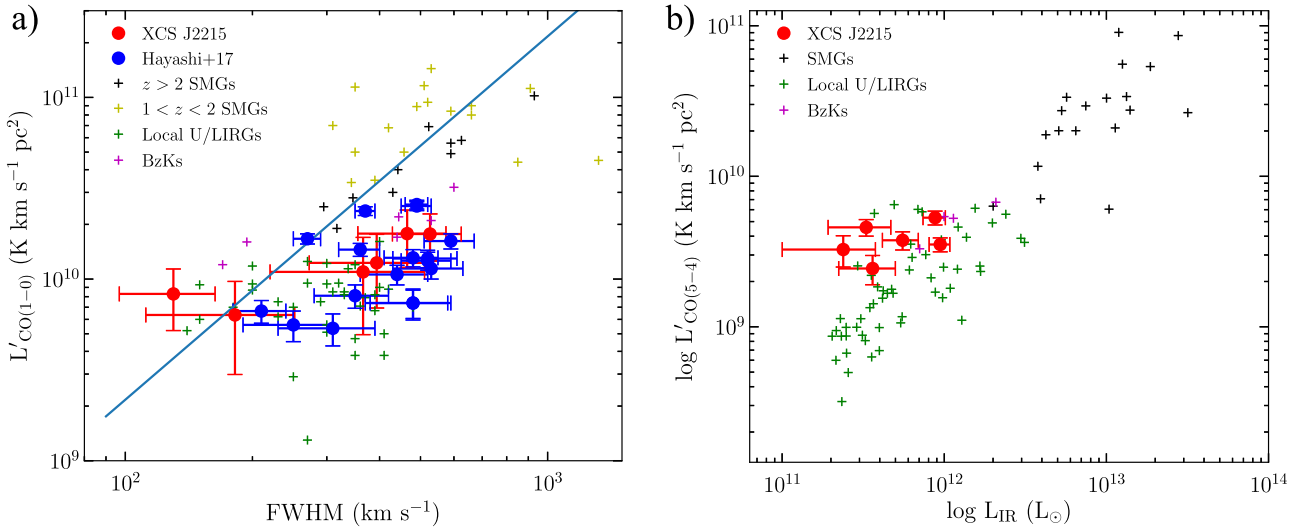

Figure 5. (a) Variation of $L'_{CO(1-0)}$ with FWHM of the line for the cluster LIRGs in this work (converting the ^{12}CO(2–1) line luminosity and FWHM) compared to the Hayashi et al. (2017) detections from the same cluster, local U/LIRGs (Downes & Solomon 1998), field SMGs from Genzel et al. (2010; Bothwell et al. 2013), and *BzK*s from Daddi et al. (2010). The solid line is the relation for $L'_{CO(1-0)}$ given in Equation (3). Our cluster LIRGs overlap with the local U/LIRG sample, although they appear to have slightly lower inferred $L'_{CO(1-0)}$ luminosities, at a fixed line width, compared to submillimeter-selected field SMGs and *BzK*s at a similar redshift. (b) The observed trend of $L'_{CO(5-4)}$ with L_{IR} for our six ^{12}CO-detected cluster LIRGs and comparison samples of local U/LIRGs, SMGs, and *BzK*s compiled by Daddi et al. (2015). Our cluster LIRGs show $L_{CO(5-4)}/L_{IR}$ ratios consistent within the spread of the local U/LIRG population.

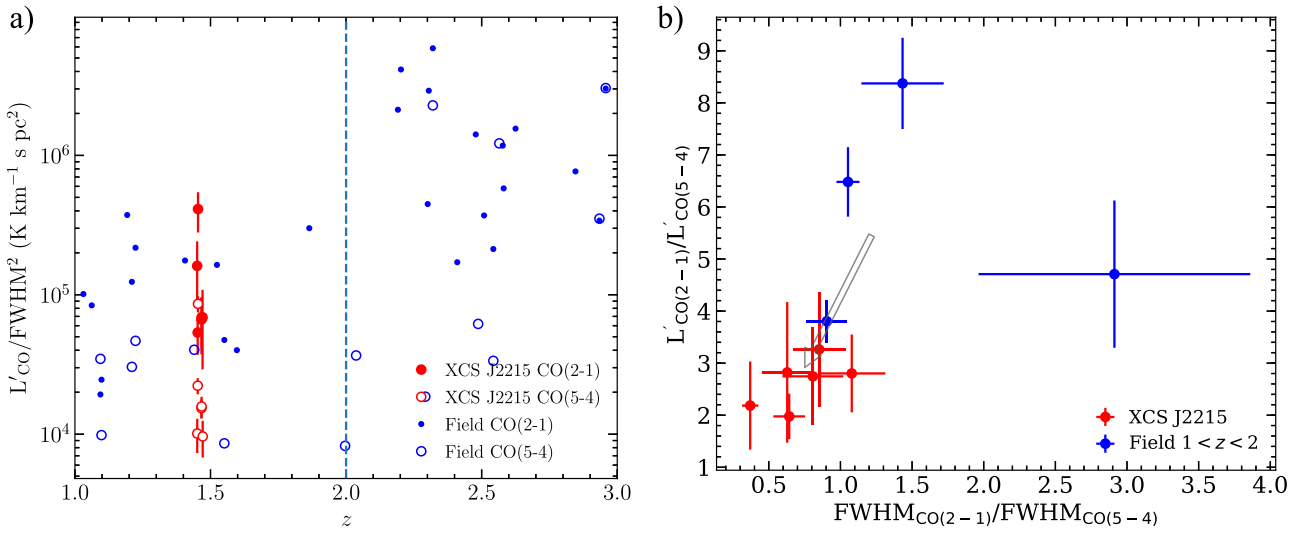

Figure 6. (a) Variation of L'_{CO}/FWHM^2 as a function of redshift. We take XCS J2215 cluster members and compare them to a field sample from the literature with published ^{12}CO(2–1) and ^{12}CO(5–4) observations. At the cluster's redshift, the galaxies with line detections show similar L'_{CO}/FWHM^2 ratios, within errors, to the field samples at their comparable redshift ($z \sim$ 1–2) for each CO transition. In the right panel, we show that it is not until you consider the ratio of L' and FWHM for the two transitions that the differences become clear. The dashed line represents our redshift cut for sample field galaxies used in the right-hand plot. (b) Plot of the ratios of the CO line luminosities against the corresponding FWHM of the two CO transitions. As in the left panel, we plot the cluster members from XCS J2215 and comparison field sources at a similar redshift from the literature which have both low-*J* CO detections ((2–1) or (1–0)) and high-*J* CO detections ((7–6), (6–5), (5–4), or (4–3)) converted to ^{12}CO(2–1) and ^{12}CO(5–4), respectively, using the brightness ratios from Bothwell et al. (2013). We see that the cluster galaxies inhabit the lower left of the plot compared to the small sample of field sources with the relevant observations, suggesting that these galaxies may be comparatively poor in lower-density, cool gas in comparison to the field sample. One possible explanation for this trend is environmental processes stripping the cooler, less-bound gas from the outskirts of the galaxies. We overlay an arrow indicating the difference in the median values of the field sample to the cluster galaxies to highlight the possible transition of a field galaxy to a cluster galaxy and the resulting effect on the low-*J* CO line properties.

environmental processing, compared to the template populations used to fit their SEDs (see Section 3.1).

4.1. Environmental Affects on the Gas and Dust in Cluster U/LIRGs

Looking at the gas and dust properties of our CO-detected galaxies in XCS J2215, we see several hints which all may be pointing to a relative paucity of cool gas and dust in these systems: (i) the galaxies typically have low ^{12}CO(2–1) luminosities at a fixed FWHM, compared to field galaxies; (ii) the line width measured from ^{12}CO(2–1) is typically smaller than that measured for ^{12}CO(5–4); (iii) at a fixed ^{12}CO(5–4) line luminosity, these galaxies have lower inferred far-infrared luminosities (which is driven primarily by 1.25 μm —rest-frame ~500 μm—flux) than comparable field galaxies. To isolate these trends in Figure 6(a), we plot L'_{CO}/FWHM^2, a proxy of gas fraction, as a function of redshift. The XCS 2215

galaxies possess similar $L'_{CO}/FWHM^2$ for both the $^{12}CO(2–1)$ and $^{12}CO(5–4)$ transitions in comparison to similar U/LIRGs in the field taken from the literature (Bothwell et al. 2013; Carilli & Walter 2013; Zavala et al. 2015; Decarli et al. 2016). In Figure 6(b), we consider the CO luminosity and FWHM ratio for these two transitions for the cluster galaxies and a sample of similar redshift field galaxies. We limit the redshift range for the field comparison sample to $z = 1–2$ to try to remove evolutionary behavior such as the increasing size of star-forming galaxies at lower redshifts (van der Wel et al. 2014), which might otherwise produce a spurious trend in $L'_{CO}/FWHM^2$ with redshift. Unfortunately, this leaves us with very few appropriate comparison sources as we are constrained by field galaxies in our redshift range that have observations in both high- and low-J CO transitions. The CO luminosity and FWHM ratios both show a tentative trend that the cluster galaxies are comparatively poorer in the lower-density, cool $^{12}CO(2–1)$ gas and also show a smaller $^{12}CO(2–1)$ FWHM, suggesting that any deficit may be occurring on the outskirts of these galaxies. This would be consistent with the stripping of the cool, lower-density gas and dust from the gas disks as a result of an environment process (e.g., ram pressure stripping) that leaves the more tightly bound, denser $^{12}CO(5–4)$ material relatively untouched (Rawle et al. 2012). However, further observations of low- and high-J CO are needed of larger samples of high-redshift cluster and field galaxies to test this suggestion.

4.2. Present Descendants of Cluster U/LIRGs

The final issue we wish to address is, what are the likely properties of the present-day descendants of these galaxies? They are bound in the cluster potential and so their stellar remnants will reside in a massive cluster of galaxies at the present day. As we have noted, while these galaxies are rapidly forming stars at $z = 1.46$ and ∼200–800 Myr later ($z \sim 1.2–1.4$, depending upon the choice of α_{CO}), this activity is likely to have declined substantially as their gas reservoirs are exhausted (this process will be even quicker if outflows or the further action of the environmental processes suggested above accelerate the removal of gas). These star formation events may form a significant fraction of the stellar mass of these systems, up to $\sim 10^{11}\,M_\odot$ (Ma15), although these estimates are highly uncertain. Hence, we can conclude that the galaxies are likely to be massive at the present day, and if their star formation terminates at $z \sim 1.2–1.4$, then their stellar populations will appear old today as this corresponds to a lookback time of ∼9 Gyr.

Clusters of galaxies have long been known to house some of the oldest and most massive galaxies seen at the present day, but we can use our (relatively obscuration-free) measures of the dynamical masses of these galaxies to compare them more directly to local early-type galaxies. The lookback time to $z = 1.46$ is 9.3 Gyr, and our expectation is that the galaxies will rapidly exhaust their current gas supplies (and are unlikely to accrete substantial amounts of cold gas from their surroundings). Hence, the stellar populations in their descendants at the present day are likely to have inferred ages of at least 9 Gyr. In addition, if we assume that the dynamical mass of the galaxies do not change significantly during the 9 Gyr, then the width of our Gaussian fits (σ_{Gauss}) can be converted into an expected velocity dispersion (σ) by comparing the ratio of our mass estimator for disks with a simple virial equation

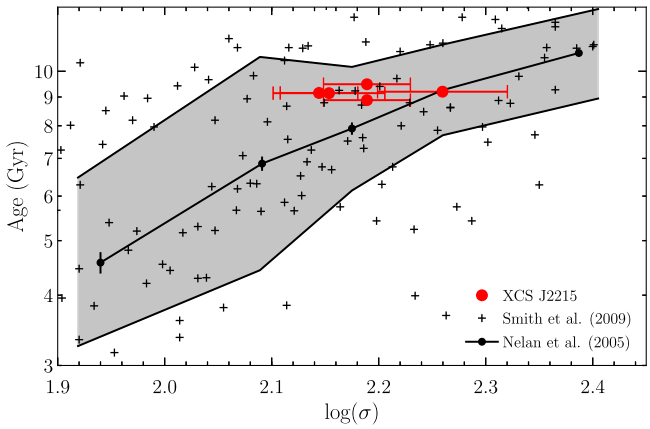

Figure 7. Plot of the velocity dispersion of local early-type galaxies to their luminosity-weighted stellar ages, adapted from Nelan et al. (2005). We show the median trend line and dispersion derived by Nelan et al. (2005) and overplot measurements for individual galaxies in the Shapley Supercluster from Smith et al. (2009) to illustrate the scatter. We plot the velocity dispersions derived from the Gaussian fits to the ^{12}CO lines for the six CO-detected millimeter members in the core of XCS J2215, where their adopted age is the lookback time to $z = 1.46$, 9.3 Gyr. These points therefore lie where they would appear today if the bulk of their stars were formed in the starburst event we are currently witnessing.

estimator for a spherical mass distribution, giving us a conversion factor of $\sigma \sim 0.3\sigma_{Gauss}$. We compare the expected properties of these galaxies to those of samples of early-type galaxies in local clusters in Figure 7. We see that most (five out of six) of the ^{12}CO-detected LIRGs in XCS J2215 have characteristics similar to those expected for the progenitors of relatively massive early-type galaxies at the present day.

5. Conclusions

We analyzed ALMA 1.25 mm and 3 mm, and MUSE-GALACSI observations of a ∼500 kpc diameter region in the core of the $z = 1.46$ cluster, XCS J2215. Our ALMA observations detect 14 luminous 1.25 mm dust continuum sources within this region (Figure 1), representing a ∼7× over-density of sources compared to a blank field. We detect line emission from six of the brightest of these sources in the 1.25 and 3 mm datacubes and associate these lines with redshifted $^{12}CO(5–4)$ and $^{12}CO(2–1)$ transitions (Figure 3). These lines unambiguously identify the millimeter sources as members of the clusters, while five other continuum sources have archival $^{12}CO(2–1)$ detections that also place them in the cluster. A further two sources have photometric redshifts compatible with them being cluster members, but lack spectroscopic redshifts from either ALMA or MUSE (consistent with the expected field contamination in this map of ∼1–2 sources). The 11 spectroscopically confirmed millimeter members have a velocity dispersion that is marginally higher than the remainder of the optical/near-infrared cluster members, hinting that they may be relatively recently accreted onto the cluster.

Together, these results indicate that the vast majority of the millimeter sources are cluster members, and they confirm the intense obscured star formation occurring in the cluster core: $\gtrsim 1000\,M_\odot\,yr^{-1}$ in a ∼500 kpc region, suggested by Ma15's earlier SCUBA-2 study. Combining our precise ALMA positions with high-resolution *HST* imaging, we see a high fraction of millimeter continuum-selected galaxies with close companions on $\lesssim 2''–3''$ scales (Figure 2), suggesting that galaxy–galaxy interactions may be a trigger for their activity,

although most of these companions are faint in the K_s band, indicating these are likely to be minor mergers/interactions.

We combine the ^{12}CO(5–4) and ^{12}CO(2–1) line fluxes for the cluster LIRGs to derive a median line brightness ratio, $r_{54/21} = L'_{\rm CO(5-4)}/L'_{\rm CO(2-1)} = 0.37 \pm 0.06$. This is comparable to the median ratio estimated for SMGs and *BzK* populations at similar and higher redshifts, indicating broadly similar gas excitation in our sample of $z = 1.46$ cluster LIRGs to these high-redshift star-forming populations (Figure 4). We estimate gas masses (assuming $\alpha_{\rm CO} = 1$) of $\sim$(1–2.5) $\times$ 10^{10} $M_{\odot}$ and a median gas consumption timescale of $\sim$200 Myr. This timescale is comparable to the time for a galaxy to cross the cluster core and so we anticipate that most of these galaxies will deplete their reservoirs before they exit the region they are currently seen in.

We also see a possible trend in terms of the gas and dust properties of the millimeter sources compared to $z \sim$ 1–2 field galaxies, which may be pointing to a relative paucity of cool gas and dust in the cluster population: (i) our XCS J2215 galaxies typically have lower ^{12}CO(2–1) luminosities compared to their FWHM than comparable field galaxies, (ii) the line width measured from ^{12}CO(2–1) is typically smaller than that measured for ^{12}CO(5–4), (iii) at a fixed ^{12}CO(5–4) line luminosity, these galaxies have lower far-infrared luminosities than comparable field galaxies, and (iv) the ratio of the ^{12}CO(2–1) and ^{12}CO(5–4) CO line luminosities and the FWHM suggest that the cluster galaxies contain a larger fraction of warmer, denser ^{12}CO(5–4) gas compared to field galaxies. These trends could be caused by the preferential removal of cooler, lower-density material as a result of an environmental process (possibly ram pressure stripping; Rawle et al. 2012). Larger samples of cluster galaxies are needed to confirm the reality of this trend.

Finally, we demonstrated that these galaxies have some of the properties of the expected progenitors of the massive, early-type galaxies that dominate the high-density regions of rich clusters of galaxies at the present day. Specifically, their dynamical masses and stellar ages roughly match those seen in early-type galaxies in local clusters.

S.M.S. acknowledges the support of an STFC studentship (ST/N50404X/1). A.M.S. and I.R.S. acknowledge financial support from an STFC (ST/L00075X/1). I.R.S. also acknowledges support from the ERC Advanced Investigator program DUSTYGAL 321334 and a Royal Society/Wolfson Merit Award. We thank Cheng-Jiun Ma, Chian-Chou Chen, Roberto Decarli, Sune Toft, Tomotsugu Goto, and Alasdair Thomson for their help with the early stages of this project. The ALMA data used in this paper were obtained under program ADS/JAO. ALMA#2015.1.00575.S and ADS/JAO.ALMA#2013.1.01213. S. ALMA is a partnership of ESO (representing its member states), NSF (USA) and NINS (Japan), together with NRC (Canada), and NSC and ASIAA (Taiwan), in cooperation with the Republic of Chile. The Joint ALMA Observatory is operated by ESO, AUI/NRAO, and NAOJ. This paper used data from projects M13AU29 and M13BU10 on the James Clerk Maxwell Telescope, which is operated by the East Asian Observatory on behalf of The National Astronomical Observatory of Japan, Academia Sinica Institute of Astronomy and Astrophysics, the Korea Astronomy and Space Science Institute, the National Astronomical Observatories of China, and the Chinese Academy of Sciences (Grant No. XDB09000000), with additional funding support from the Science and Technology Facilities Council of the United Kingdom and participating universities in the United Kingdom and Canada. The MUSE data are based on observations made with ESO Telescopes at the La Silla Paranal Observatory under programme 60.A-9180. All of the data used here are available through the ESO, ALMA, and *HST* archives or in published papers.

ORCID iDs

Stuart M. Stach https://orcid.org/0000-0003-1122-6948
A. M. Swinbank https://orcid.org/0000-0003-1192-5837
Ian Smail https://orcid.org/0000-0003-3037-257X
Matt Hilton https://orcid.org/0000-0002-8490-8117
J. M. Simpson https://orcid.org/0000-0002-8521-1995
E. A. Cooke https://orcid.org/0000-0003-3843-8393

References

Aguilar, L. A., & White, S. 1985, ApJ, 295, 374
Aragón-Salamanca, A., Ellis, R. S., Couch, W. J., & Carter, D. 1993, MNRAS, 262, 764
Aravena, M., Decarli, R., Walter, F., et al. 2016, ApJ, 833, 68
Balogh, M., Eke, V., Miller, C., et al. 2004, MNRAS, 348, 1355
Bamford, S. P., Nichol, R. C., Baldry, I. K., et al. 2009, MNRAS, 393, 1324
Biviano, A., Fadda, D., Durret, F., Edwards, L., & Marleau, F. 2011, A&A, 532, A77
Bolatto, A. D., Wolfire, M., & Leroy, A. K. 2013, ARA&A, 51, 207
Bothwell, M., Smail, I., Chapman, S., et al. 2013, MNRAS, 429, 3047
Bournaud, F., Daddi, E., Weiß, A., et al. 2015, A&A, 575, A56
Bower, R. G., Lucey, J., & Ellis, R. S. 1992, MNRAS, 254, 589
Brodwin, M., Stanford, S., Gonzalez, A. H., et al. 2013, ApJ, 779, 138
Butcher, H., & Oemler, A., Jr. 1978, ApJ, 226, 559
Carilli, C., & Walter, F. 2013, ARA&A, 51, 105
Carlberg, R., Yee, H., & Ellingson, E. 1997, ApJ, 478, 462
Chabrier, G. 2003, PASP, 115, 763
Chary, R., & Elbaz, D. 2001, ApJ, 556, 562
Cowie, L. L., Barger, A., Fomalont, E., & Capak, P. 2004, ApJL, 603, L69
da Cunha, E., Walter, F., Smail, I., et al. 2015, ApJ, 806, 110
Daddi, E., Bournaud, F., Walter, F., et al. 2010, ApJ, 713, 686
Daddi, E., Dannerbauer, H., Liu, D., et al. 2015, A&A, 577, A46
Darvish, B., Mobasher, B., Sobral, D., et al. 2016, ApJ, 825, 113
Dawson, K., Aldering, G., Amanullah, R., et al. 2009, AJ, 138, 1271
Decarli, R., Walter, F., Aravena, M., et al. 2016, ApJ, 833, 69
Downes, D., & Solomon, P. 1998, ApJ, 507, 615
Draine, B., Dale, D., Bendo, G., et al. 2007, ApJ, 663, 866
Dressler, A. 1980, ApJ, 236, 351
Dunlop, J. S., McLure, R., Biggs, A., et al. 2016, MNRAS, 466, 861
Engel, H., Tacconi, L., Davies, R., et al. 2010, ApJ, 724, 233
Fadda, D., Biviano, A., Marleau, F. R., Storrie-Lombardi, L. J., & Durret, F. 2007, ApJL, 672, L9
Finn, R. A., Desai, V., Rudnick, G., et al. 2010, ApJ, 720, 87
Fixsen, D. J., Bennett, C., & Mather, J. C. 1999, ApJ, 526, 207
Geach, J., Smail, I., Ellis, R., et al. 2006, ApJ, 649, 661
Genzel, R., Tacconi, L., Gracia-Carpio, J., et al. 2010, MNRAS, 407, 2091
Genzel, R., Tacconi, L., Lutz, D., et al. 2015, ApJ, 800, 20
Gomez, P. L., Nichol, R. C., Miller, C. J., et al. 2003, ApJ, 584, 210
Gunn, J. E., & Gott, J. R., III. 1972, ApJ, 176, 1
Haines, C., Smith, G., Egami, E., et al. 2009, ApJ, 704, 126
Hancock, P. J., Murphy, T., Gaensler, B. M., Hopkins, A., & Curran, J. R. 2012, MNRAS, 422, 1812
Hatch, N. A., Cooke, E. A., Muldrew, S. I., et al. 2016, MNRAS, 464, 876
Hayashi, M., Kodama, T., Kohno, K., et al. 2017, ApJL, 841, L21
Hayashi, M., Kodama, T., Koyama, Y., et al. 2010, MNRAS, 402, 1980
Hayashi, M., Kodama, T., Koyama, Y., et al. 2014, MNRAS, 439, 2571
Hilton, M., Collins, C. A., Stanford, S. A., et al. 2007, ApJ, 670, 1000
Hilton, M., Lloyd-Davies, E., Stanford, S. A., et al. 2010, ApJ, 718, 133
Hilton, M., Stanford, S. A., Stott, J. P., et al. 2009, ApJ, 697, 436
Ivison, R., Papadopoulos, P., Smail, I., et al. 2011, MNRAS, 412, 1913
Kennicutt, R. 1998, ARA&A, 36, 189
Kodama, T., Yamada, T., Akiyama, M., et al. 2004, MNRAS, 350, 1005
Larson, R., Tinsley, B., & Caldwell, C. 1980, ApJ, 237, 692

Lewis, I., Balogh, M., De Propris, R., et al. 2002, MNRAS, 334, 673
Lotz, J. M., Papovich, C., Faber, S., et al. 2013, ApJ, 773, 154
Ma, C.-J., Smail, I., Swinbank, A., et al. 2015, ApJ, 806, 257
McMullin, J., Waters, B., Schiebel, D., Young, W., & Golap, K. 2007, in ASP Conf. Ser. 376, Astronomical Data Analysis Software and Systems XVI, ed. R. A. Shaw, F. Hill, & D. J. Bell (San Fransico, CA: ASP), 127
Merritt, D. 1983, ApJ, 264, 24
Narayanan, D., Krumholz, M. R., Ostriker, E. C., & Hernquist, L. 2012, MNRAS, 421, 3127
Nelan, J. E., Smith, R. J., Hudson, M. J., et al. 2005, ApJ, 632, 137
Newman, A. B., Ellis, R. S., Andreon, S., et al. 2014, ApJL, 788, 51
Noble, A., Webb, T., Yee, H., et al. 2016, ApJ, 816, 48
Oteo, I., Zwaan, M. A., Ivison, R. J., Smail, I., & Biggs, A. D. 2016, ApJ, 822, 36
Papadopoulos, P., Ivison, R., Carilli, C., & Lewis, G. 2001, Natur, 409, 58
Papadopoulos, P. P., van der Werf, P. P., Xilouris, E., et al. 2012, MNRAS, 426, 2601
Popesso, P., Biviano, A., Rodighiero, G., et al. 2012, A&A, 537, A58
Rawle, T., Rex, M., Egami, E., et al. 2012, ApJ, 756, 106
Rieke, G. H., Alonso-Herrero, A., Weiner, B., et al. 2009, ApJ, 692, 556
Rudnick, G. H., Tran, K.-V., Papovich, C., Momcheva, I., & Willmer, C. 2012, ApJ, 755, 14
Saintonge, A., Tran, K.-V. H., & Holden, B. P. 2008, ApJL, 685, L113
Santos, J., Altieri, B., Popesso, P., et al. 2013, MNRAS, 433, 1287
Santos, J. S., Altieri, B., Valtchanov, I., et al. 2015, MNRAS Lett., 447, L65
Smail, I., Geach, J., Swinbank, A., et al. 2014, ApJ, 782, 19
Smith, R. J., Lucey, J. R., & Hudson, M. J. 2009, MNRAS, 400, 1690
Solomon, P., & Vanden Bout, P. 2005, ARA&A, 43, 677
Stanford, S., Romer, A. K., Sabirli, K., et al. 2006, ApJL, 646, L13
Swinbank, A., Simpson, J., Smail, I., et al. 2013, MNRAS, 438, 1267
Tacconi, L., Neri, R., Genzel, R., et al. 2013, ApJ, 768, 74
Tran, K.-V. H., Papovich, C., Saintonge, A., et al. 2010, ApJL, 719, L126
van der Wel, A., Franx, M., Van Dokkum, P., et al. 2014, ApJ, 788, 28
Wang, T., Elbaz, D., Daddi, E., et al. 2016, ApJ, 828, 56
Webb, T., O'Donnell, D., Yee, H. K., et al. 2013, ApJ, 146, 84
Webb, T., Yee, H., Ivison, R., et al. 2005, ApJ, 631, 187
Whitmore, B. C., Gilmore, D. M., & Jones, C. 1993, ApJ, 407, 489
Zavala, J., Yun, M., Aretxaga, I., et al. 2015, MNRAS, 452, 1140